**ADVANCED
MATERIALS**

www.advmat.de

Stable High-Index Faceted Pt Skin on Zigzag-Like PtFe Nanowires Enhances Oxygen Reduction Catalysis

Mingchuan Luo, Yingjun Sun, Xu Zhang, Yingnan Qin, Mingqiang Li, Yingjie Li, Chunji Li, Yong Yang, Lei Wang, Peng Gao, Gang Lu, and Shaojun Guo*

Selectively exposing active surfaces and judiciously tuning the near-surface composition of electrode materials represent two prominent means of promoting electrocatalytic performance. Here, a new class of Pt_3Fe zigzag-like nanowires (Pt-skin Pt_3Fe z-NWs) with stable high-index facets (HIFs) and nanosegregated Pt-skin structure is reported, which are capable of substantially boosting electrocatalysis in fuel cells. These unique structural features endow the Pt-skin Pt_3Fe z-NWs with a mass activity of 2.11 A mg^{-1} and a specifc activity of 4.34 mA cm^{-2} for the oxygen reduction reaction (ORR) at 0.9 V versus reversible hydrogen electrode, which are the highest in all reported PtFe-based ORR catalysts. Density function theory calculations reveal a combination of exposed HIFs and formation of Pt-skin structure, leading to an optimal oxygen adsorption energy due to the ligand and strain effects, which is responsible for the much enhanced ORR activities. In contrast to previously reported HIFs-based catalysts, the Pt-skin Pt_3Fe z-NWs maintain ultrahigh durability with little activity decay and negligible structure transformation after 50 000 potential cycles. Overcoming a key technical barrier in electrocatalysis, this work successfully extends the nanosegregated Pt-skin structure to nanocatalysts with HIFs, heralding the exciting prospects of high-effcient Pt-based catalysts in fuel cells.

Proton exchange membrane fuel cells (PEMFCs) are widely considered as the ideal alternative to conventional internal combustion engine in areas of transportation, and stationary and portable power generation owing to their potential to solve the global problems of energy supply and environmental concern.[1–4] However, the wide deployment of PEMFCs is hindered by the sluggish kinetics of oxygen reduction reaction (ORR) at cathode even when the best metal catalyst (Pt) is used.[5–9] To overcome this obstacle, it is crucial to develop inexpensive catalysts with much higher ORR activities.[10,11]

An attractive strategy to boost ORR activity on Pt-based catalysts is to introduce a second transition metal (M) and to judiciously tailor the near-surface composition and structure, taking advantage of favorable ligand and strain effects to boost ORR activity.[12–15] For example, previous studies have identified a nanosegregated Pt-skin structure to be extremely active

Dr. M. C. Luo, Dr. Y. J. Sun, Y. N. Qin, Dr. Y. J. Li, Dr. C. J. Li,
Dr. Y. Yang, Prof. S. J. Guo
Department of Materials Science & Engineering
College of Engineering
Peking University
Beijing 100871, China
E-mail: guosj@pku.edu.cn
Dr. Y. J. Sun, Y. N. Qin, Prof. L. Wang
College of Chemistry and Molecular Engineering
Qingdao University of Science and Technology
Qingdao 266042, China
Dr. X. Zhang, Prof. G. Lu
Department of Physics and Astronomy
California State University
Northridge, CA 91330, USA
Dr. M. Q. Li, Prof. P. Gao
Electron Microscopy Laboratory
and International Center for Quantum Materials
School of Physics
Peking University
Beijing 100871, China

Dr. M. Q. Li
Academy for Advanced Interdisciplinary Studies
Peking University
Beijing 100871, China
Prof. P. Gao
Collaborative Innovation Centre of Quantum Matter
Beijing 100871, China
Prof. S. J. Guo
BIC-ESAT
College of Engineering
Peking University
Beijing 100871, China
Prof. S. J. Guo
Department of Energy and Resources Engineering
College of Engineering
Peking University
Beijing 100871, China
Prof. S. J. Guo
Beijing Key Laboratory for Magnetoeletric Materials and Devices (BKL-MEMD)
Peking University
Beijing 100871, China

**ADVANCED
SCIENCE NEWS**

www.advancedsciencenews.com

**ADVANCED
MATERIALS**

www.advmat.de

for ORR. By exposing Pt-skin Pt_3Ni with three typical low-index facets (111), (100), and (110), the (111) faceted Pt-skin Pt_3Ni delivers much higher ORR activity than the (100) and (110) faceted one, and nearly two orders of magnitude higher ORR specific activity than the state-of-the-art carbon supported Pt nanoparticles (Pt/C).[16] To date, much research has been devoted to transferring the unique (111) faceted Pt_3M skin onto practical nanocatalysts, leading to the development of promising Pt-based nanocatalysts shaped in octahedron,[17–21] icosahedron,[22] and nanoframe.[23–25] These studies not only demonstrate the importance of inducing nanosegregated Pt-skin structure but also suggest the strong dependence of ORR electrocatalysis on the exposed Pt facets.[26] Since the intrinsic ORR activity on Pt single-crystal thin film follows the ranking: high-index facets (HIFs) > (111) > (100),[6,27,28] one would expect that by creating HIF Pt skin on the surface of Pt_3M nanocrystal would lead to enhanced ORR activity. However, higher surface energies of the HIFs render such structures unlikely to be achieved, especially during thermal annealing process necessary for the formation of the Pt-skin structure.[29] Another critical concern is that even if such desirable structure could be formed, maintaining it under the operational condition of fuel cells poses a great challenge.

Taking these challenges head on, we are able to produce an extremely stable HIF Pt skin onto 1D Pt_3Fe zigzag-like nanowires (NWs), delivering much more active and durable ORR catalysis. The Pt-skin Pt_3Fe zigzag-like NWs (denoted as Pt-skin Pt_3Fe z-NWs) were prepared by first simultaneously reducing the Pt and Fe precursors to yield Pt_3Fe z-NWs, and subsequently thermally annealing the z-NWs at high temperature (see the Supporting Information for details). Compared to typical nanoparticulate morphologies, the 1D z-NWs are highly unusual with a HIF Pt skin, stemming from their anisotropic nature. This unique 1D catalyst enables an unprecedented ORR mass activity of 2.11 A mg^{-1} and a specific activity of 4.34 mA cm^{-2}, which are the highest among all the reported PtFe-based catalysts, at 0.9 V versus reversible hydrogen electrode (RHE), far exceeding those of commercial Pt/C catalyst and the technique target set by the U.S. DOE. Density function theory (DFT) calculations reveal that the strong ligand and strain effect resulted from a combination of exposed HIFs and Pt-skin structure leads to optimal oxygen adsorption energy, giving rise to much enhanced ORR activity. Surprisingly, the HIFs enclosed Pt-skin Pt_3Fe z-NWs are also electrochemically stable under electrocatalytic conditions, with little activity decay and negligible structure transformation after a long-term course of 50 000 potential cycles. Meanwhile, the Pt-skin Pt_3Fe z-NWs/C also shows significantly improved catalytic performance toward the anodic methanol/ethanol oxidation reaction (MOR/EOR) over the pristine Pt_3Fe z-NWs/C and commercial Pt/C counterparts.

A facile wet-chemical approach was used to synthesize Pt_3Fe z-NWs by using platinum (II) acetylacetonate (Pt(acac)$_2$) and iron(III) acetylacetonate (Fe(acac)$_3$) as the metal precursors, glucose as the reducing agent, cetyltrimethylammonium chloride (CTAC) as the surfactant, and oleylamine as the solvent. Control experiments were carried out to identify the optimal synthetic parameters for the Pt_3Fe z-NWs by tuning the feeding ratios of metal precursors, the amount of glucose and CTAC. We found that a proper amount of reducing agent (glucose) and surfactant (CTAC), which controls the kinetics of nucleation and growth of nanocrystals,[30,31] is the key to the formation of 1D nanostructures (Figures S1 and S2, Supporting Information). In addition, the feeding ratio of Pt to Fe precursors has little influence on the final composition of Pt_3Fe z-NWs, but largely impacts the Zigzag-like structure of NWs (Figures S3 and S4, Supporting Information).

The morphology of as-synthesized Pt_3Fe z-NWs was characterized by transmission electron microscopy (TEM) and high-angle annular dark-field scanning transmission electron microscopy (HAADF-STEM). As shown in **Figure 1**a,b, 1D z-NWs enclosed by highly uneven surfaces were the dominant product. They have the lengths of hundreds of nanometers and diameters of around 10 nm, leading to an average aspect ratio of 40. The composition of Pt to Fe in z-NWs was determined to be 76.2/23.8 by the STEM energy-dispersive X-ray spectroscopy (STEM-EDS) (Figure 1c), in accordance with the result from inductively coupled plasma-atomic emission spectroscopy (ICP-AES). The Pt_3Fe z-NWs have a face-centered cubic (fcc) structure, as revealed by the powder X-ray diffraction (PXRD) pattern (Figure 1d). The main diffraction peaks of Pt_3Fe z-NWs are located between those of fcc Pt (JCPDS No. 04-0802) and fcc Fe (JCPDS No. 52-0513), suggesting the formation of alloys.[32] The STEM-EDS mapping of single Pt_3Fe z-NW reveals the homogeneous distribution of Pt and Fe throughout the NW without notable composition segregation (Figure 1e), indicating typical solid solution phase of Pt_3Fe z-NWs. We further used aberration-corrected STEM to characterize the atomic structure of Pt_3Fe z-NWs along the zone axis of [110], and found the uneven surface of z-NWs was dominated by HIFs, such as (311) and (211) facets, that were previously reported to be highly desirable for electrocatalysis (Figure S5, Supporting Information).[33]

To minimize agglomeration or sintering, we first deposited free-standing Pt_3Fe z-NWs (dispersed in cyclohexane) onto high-surface carbon black (C, EC-300) via sonication, and subsequently treated the carbon supported Pt_3Fe z-NWs (Pt_3Fe z-NWs/C) at temperatures of 370, 400, 430, and 460 °C, which are the commonly used temperatures to induce nanosegregated Pt-skin structure. Although the 1D z-NWs showed excellent antiaggregation property upon thermal annealing,[34] the crystalline size of Pt_3Fe z-NWs was found to increase slightly with the applied annealing temperature, as verified by the temperature-dependent PXRD (Figure S6, Supporting Information). The phenomenon of surface smoothing, indicative of the disappearance of HIFs, was also observed on Pt_3Fe z-NWs being treated at temperature above 430 °C (Figure S7, Supporting Information). Therefore, 400 °C is considered as the optimal temperature for the formation of Pt-skin Pt_3Fe z-NWs.

Figure 2a shows the typical STEM image of Pt-skin Pt_3Fe z-NWs that were subject to 400 °C for 2 h. Numerous (311) and (211) facets could still be identified on the surface of Pt-skin Pt_3Fe z-NWs, as confirmed by the high-magnification STEM image (Figure 2b,d and Figure S8, Supporting Information), indicating highly thermal durability of HIFs on NWs. High-resolution STEM-EDS elemental mapping analysis further reveals the formation of an ultrathin Pt shell on the surface of as-annealed sample, indicating the production of Pt-skin structure (Figure 2e). The line scan profile of single annealed Pt_3Fe z-NW further confirms the presence of an ultrathin Pt shell
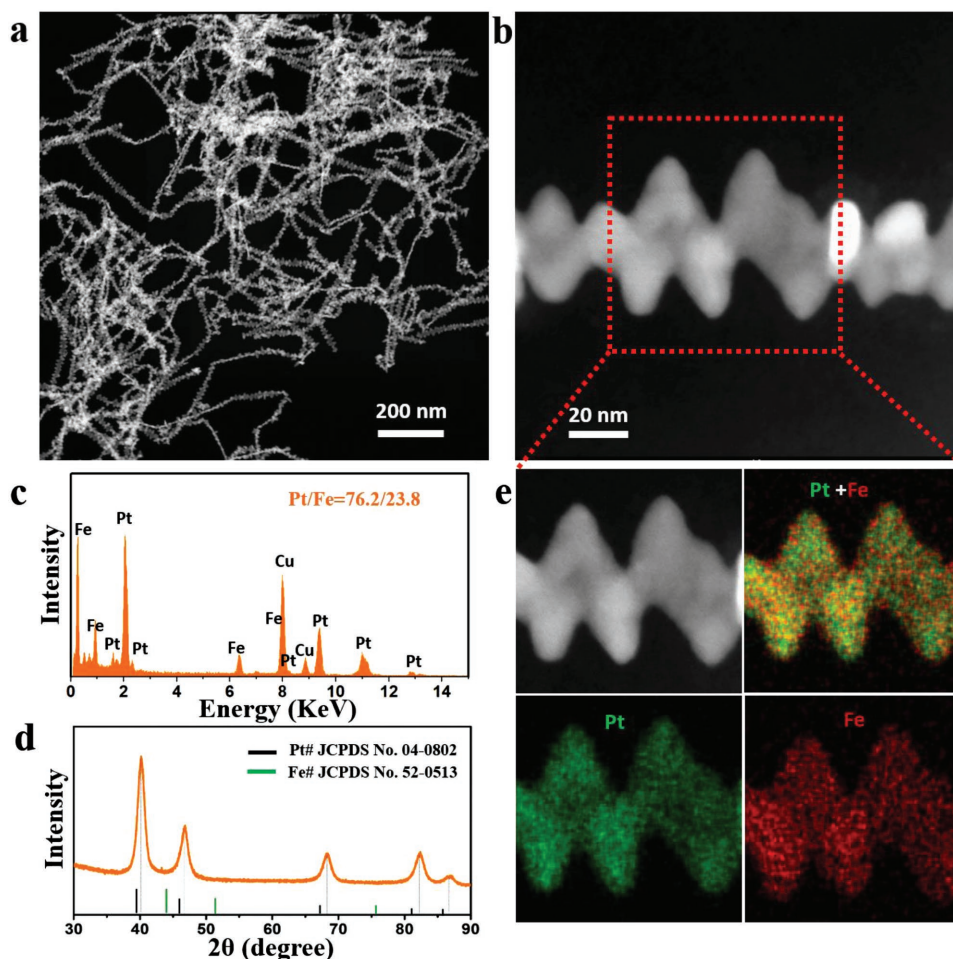
**ADVANCED
SCIENCE NEWS**

www.advancedsciencenews.com

**ADVANCED
MATERIALS**

www.advmat.de

Figure 1. Structural and compositional characterizations of Pt_3Fe zigzag-like nanowires. a) Low- and b) high-magnification HAADF-STEM images, c) TEM-EDS, d) PXRD pattern and e) STEM-EDS elemental mapping of Pt_3Fe z-NWs.

(Figure S9, Supporting Information). Notably, the thickness of "Pt skin" is around 0.5 nm, which is equivalent to two atomic layers rather than the typical one atomic layer observed in the single crystal electrode.[35,36] Based on these observations, we then conclude the Pt-skin Pt_3Fe z-NWs have a new class of HIF Pt skin with two atomic layers thickness.

The electrochemical performance of Pt-skin Pt_3Fe z-NWs/C, Pt_3Fe z-NWs/C and commercial Pt/C was evaluated using thin film rotating disk electrode method in a three-electrode cell. Before evaluation, it is necessary to remove excess OAm, detrimental to electrocatalysis, from the surface of pristine Pt_3Fe z-NWs.[37] Herein, a thermal treatment was adopted by annealing the pristine Pt_3Fe z-NWs/C at 220 °C for 1 h in air atmosphere,[38] rather than acidic treatment, to avoid any damage to either the structure or composition. TEM and ICP-AES analysis show that the Pt_3Fe NWs are uniformly deposited on the carbon support without structural transformation or compositional change after such treatment (Figure S10, Supporting Information). Figure S11 (Supporting Information) shows cyclic voltammograms (CVs) of various catalysts at a scan rate of 50 mV s^{-1} in N_2-saturated 0.1 M $HClO_4$. From the charge of H_{upd} desorption peak in the recorded CV, we first evaluated the electrochemically active surface area (ECSA) of

each catalyst assuming a charge density of 210 µC cm^{-2} for one monolayer of hydrogen desorption on Pt. The $ECSA_{Hupd}$ (determined by H_{upd} method) of commercial Pt/C was 59.8 m^2 g^{-1}, in reasonable agreement with the literature values, but much larger than those of Pt_3Fe z-NWs/C (43.2 m^2 g^{-1}) and Pt-skin Pt_3Fe z-NWs/C (34.0 m^2 g^{-1}). However, the H_{upd} behavior of Pt was reported to be highly sensitive to its chemical environments, especially when alloying with a nonnoble transition metal that has strong electronic interaction with Pt, and thus alter the adsorptive strength between hydrogen and Pt.[39] Normally, the ECSAs of Pt-based alloy catalysts would be underestimated by means of H_{upd} method due to a suppression of H_{upd} adsorption/desorption.[40] Thus, to avoid such underestimation, we further adopted the charge of CO stripping (oxidation of adsorbed CO) to evaluate the ECSA of each catalyst because the binding of CO molecules on Pt is so strong that the alloying effect can be neglected.

The CO stripping curves were recorded at a scan rate of 20 mV s^{-1} in N_2-saturated $HClO_4$ after the working electrodes were preadsorbed with CO for 10 min (Figure S12, Supporting Information). As listed in Table S1 (Supporting Information), the ECSA trend determined from CO stripping method ($ECSA_{CO}$) is identical to that of $ECSA_{Hupd}$: commercial
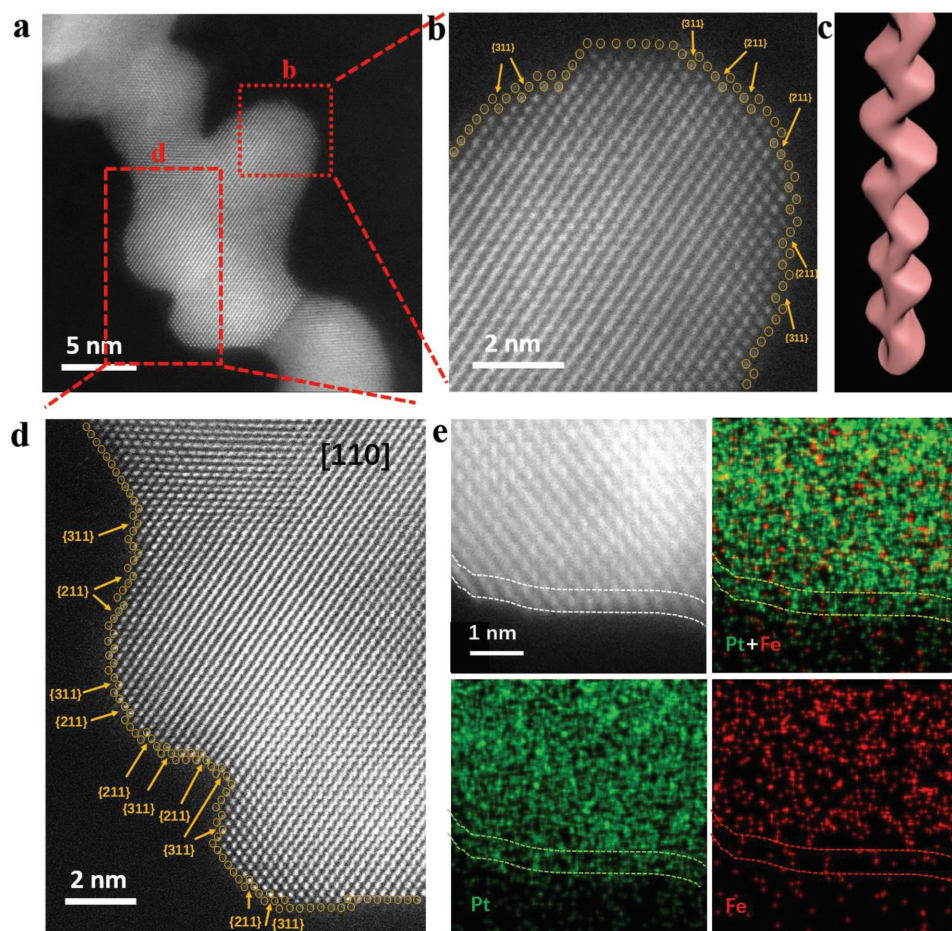
Figure 2. Structural and compositional characterizations of Pt-skin Pt_3Fe zigzag-like nanowires. a) HAADF-STEM image of Pt-skin Pt_3Fe z-NWs. b,d) The enlarged images of red square in (a). c) Structural demonstration of the z-NWs. e) STEM-EDS elemental mapping of Pt-skin Pt_3Fe z-NWs, clearly showing the presence of a "Pt skin" in around two-atomic-layer thickness on the surface. The crystal orientation of the structure is along the zone axis of [110].

Pt/C > Pt_3Fe z-NWs/C > Pt-skin Pt_3Fe z-NW/C. The well-known knowledge is that the ratio between $ECSA_{CO}$ and $ECSA_{Hupd}$ can be used to probe the near-surface structure and composition of Pt-based alloy catalyst, and a ratio of ≈1.5 is indicative of the unique nanosegregated Pt-skin structure.[39] In this study, the ratio of $ECSA_{CO}/ECSA_{Hupd}$ for commercial Pt/C, Pt_3Fe z-NWs/C and Pt-skin Pt_3Fe z-NWs/C was determined to be 1.04, 1.27, and 1.48, respectively. The distinct $ECSA_{CO}/ECSA_{Hupd}$ ratio, along with the high-resolution EDS elemental mapping and line scan analysis, strongly suggests the formation of Pt skin (two atomic layer thick) on the surface of thermal annealed Pt_3Fe z-NWs.

Figure S13 (Supporting Information) compares the polarization curves of various catalysts for ORR, normalized by geometric area of the glassy carbon electrode (0.196 cm^2). Both Pt_3Fe z-NWs/C and Pt-skin Pt_3Fe z-NWs/C show obviously positive shift in the half-wave potential ($E_{1/2}$) for ORR than that of commercial Pt/C, indicating their enhanced ORR electrocatalytic activities. To provide a more quantitative comparison on the intrinsic ORR activity, the specific activity of each catalyst was evaluated through normalizing the kinetic current (calculating from the Koutechy–Levich equation) by corresponding specific area determined from the charge of CO stripping. Plotting the specific activity as a function of applied potentials yields the Tafel plots for various catalysts (**Figure 3**a). Pt-skin Pt_3Fe z-NWs/C shows a Tafel slope of 76 mV decade^{-1}, lower than those of Pt_3Fe z-NWs/C (83 mV decade^{-1}) and Pt/C (92 mV decade^{-1}), indicating its faster kinetics toward ORR than the other two catalysts. Remarkably, the Pt-skin Pt_3Fe z-NWs/C catalyst shows the highest specific and mass activities of 4.34 mA cm^{-2} and 2.11 A mg^{-1} at 0.9 V versus RHE in all reported PtFe-based nanocatalysts (Table S2, Supporting Information), which are 16.7 and 13.2 times, and 2.1 and 1.9 times higher than those of Pt/C and Pt_3Fe z-NWs/C, respectively. The impressive activity enhancement should be largely ascribed to the unique structural feature: HIF Pt-skin structure. Notably, the mass activity of Pt-skin Pt_3Fe z-NWs/C far exceeds the 2020 target set by the U.S. DOE (0.44 A mg$_{Pt}^{-1}$, indicated by green triangle in Figure 3b).

We also investigated the influence of HIFs on the ORR activity. As shown in Figure S14 (Supporting Information), the ORR activity of the former catalyst (400 °C) was still higher than that of the latter one (≥ 430 °C), probably due to an excellent balance on the formation of Pt-skin structure and the reservation
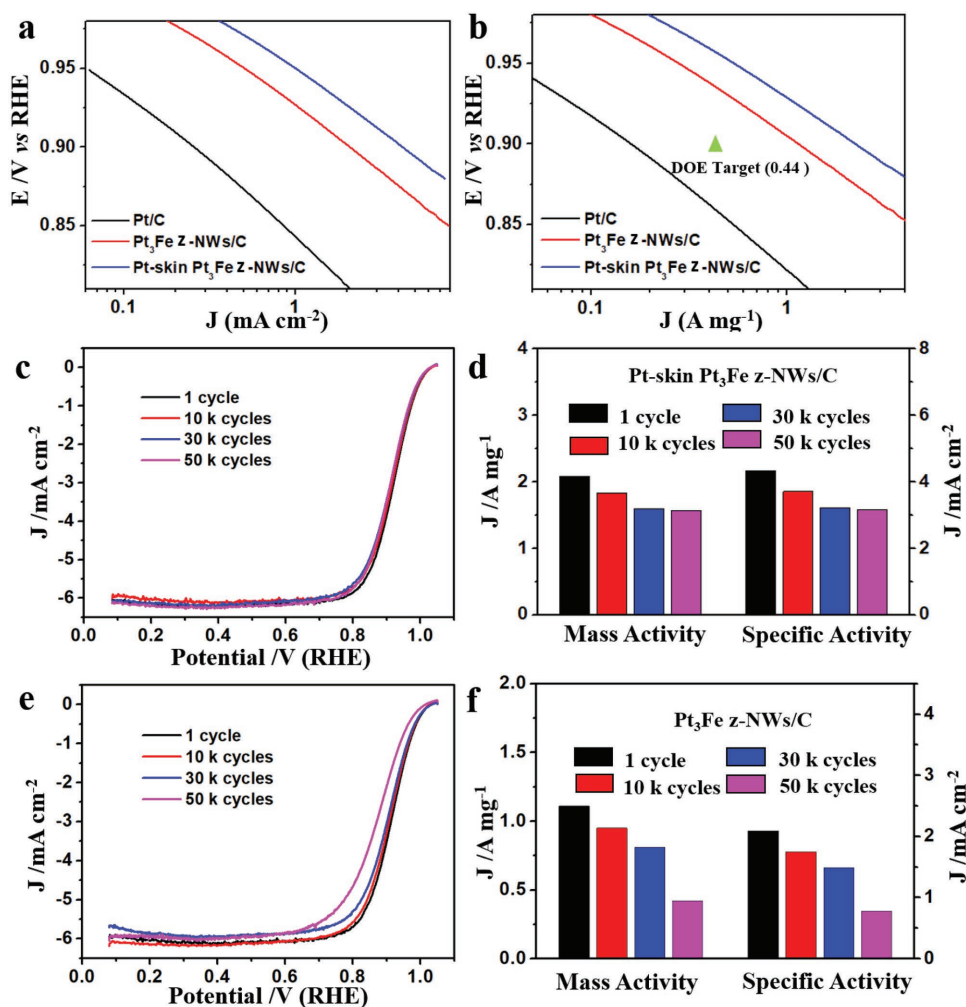
Figure 3. Catalytic performance for ORR. a) Specific activity (SA) and b) mass activity (MA) Tafel plot for commercial Pt/C, Pt₃Fe z-NWs/C, and Pt-skin Pt₃Fe z-NWs/C. Green triangle in (b) indicates the technical target for ORR set by the U.S. DOE. c) ORR polarization curves, and d) histogram of SA and MA of Pt-skin Pt₃Fe z-NWs/C before and after 10 000, 30 000, and 50 000 potential cycles between 0.6 and 1.1 V versus RHE. e) ORR polarization curves, and f) histogram of SA and MA of the pristine Pt₃Fe z-NWs/C before and after 10 000, 30 000, and 50 000 potential cycles between 0.6 and 1.1 V versus RHE.

of zigzag-like structure, confirming the importance of HIFs exposed on the surface in promoting the ORR catalytic rates. Even though the feeding ratio of Pt/Fe precursor has little influence on the composition of resultant z-NWs, we found the ORR activity is strongly depended on such feeding ratio, with a Pt/Fe ratio of 3/1 showing the highest activity (Figure S15, Supporting Information).

The key challenge that hinders the practical application of HIFs enclosed catalysts is their poor durability, because the HIFs are thermodynamic unstable due to their high surface energies.[41] Surprisingly, the Pt-skin Pt₃Fe z-NWs/C enables superior durability for ORR electrocatalysis. Figure 3c shows the ORR polarization curves of Pt-skin Pe₃Fe NWs/C before and after various potential cycles between 0.6 to 1.1 V versus RHE, which almost overlap each other. After 50 000 potential cycles, the specific activity and mass activity decreased by only 26.7% and 24.6%, respectively (Figure 3d). For the pristine Pt₃Fe z-NWs/C catalyst, the ORR activity can be fairly maintained for a short term, as evident from the negligible shift in polarization

curves and small decrease in specific activity and mass activity after a course of 30 000 cycles (Figure 3e). However, prolonging the durability test to 50 000 cycles results in a rapid decay in ORR activity, with a 62.7% loss in specific activity and a 62.2% loss in mass activity, respectively (Figure 3f). In sharp contrast, the benchmark Pt/C suffered disastrous decay in both specific activity (96.7% loss) and mass activity (93.3% loss; Figure S16, Supporting Information) after the same cycling condition.

The superior durability of Pt-skin Pt₃Fe z-NWs/C can be ascribed to several factors related to its unique structure: (1) 1D geometry of NWs enables multipoint contacts with the carbon support, which can effectively reduce the chance of movement, aggregation, detachment and ripening.[42,43] By comparing the ECSAs and TEM image of various catalysts after durability test, the NWs catalysts experienced neither decrease in ECSAs nor changes in morphology or structure, whereas severe aggregation and growth of nanoparticles were found in commercial Pt/C catalyst (Figures S17–S19, Supporting Information). Especially, the HIFs were well-maintained on the surface after the
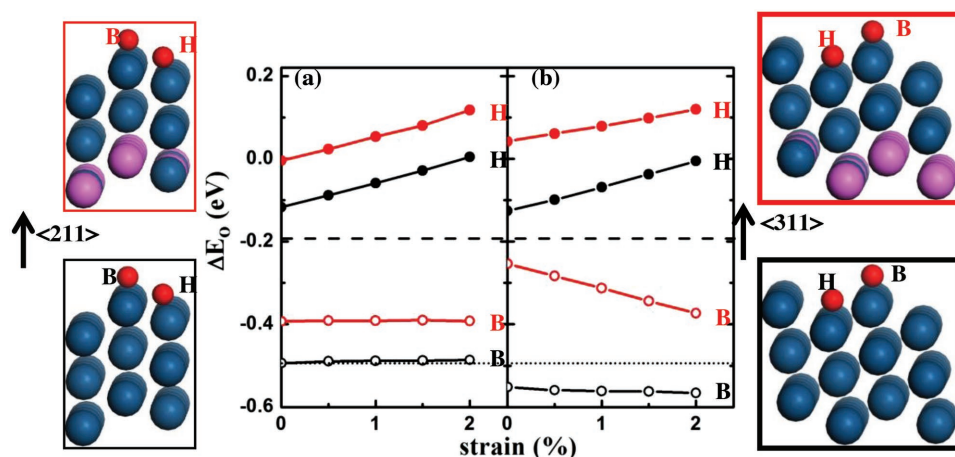
Figure 4. DFT calculation of oxygen adsorption energy. ΔE_O as a function of compressive strain on a) (211) and b) (311) surfaces. "H" and "B" indicate that the O atom is adsorbed on the fcc hollow site of the facet and the bridge site of the step edge, respectively. The filled circles represent ΔE_O values on the H site while the open circles represent those on the B site. The black and red curves correspond to ΔE_O values on the pure Pt and Pt-skin Pt_3Fe surfaces. The dashed and dotted horizontal lines indicate ΔE_O values on the (111) facet and the edge of a cuboctahedra Pt nanoparticle with a diameter of 3.5 nm.

durability tests (Figure S20, Supporting Information). (2) 1D nature and large size of NWs (10 nm in diameter and several hundred nm in length) can help relax the intrinsic high surface energies of HIFs, thus contributing significantly to their durability.[31] (3) The thickness of Pt skin was about 0.5 nm, which was equivalent to two atomic layers rather than the typical one atomic layer observed in the single crystal electrode. The forming Pt layer is crucial to maintain the high activity during long-term operation by effectively preventing the dissolution of beneficial Fe atoms.[44,45] This can be verified by the comparison in ORR activities and compositions of Pt-skin NWs and pristine NWs under different durability test stages (Figure S19, Supporting Information).

To understand the exceptional ORR performance of the Pt-skin Pt_3Fe z-NWs, we performed DFT calculations of the NWs, focusing on oxygen adsorption energy (E_O), which is an excellent descriptor for ORR activity.[46,47] There exists an optimal E_O value under which the ORR activity of the catalyst reaches the maximum. It turns out that the optimal E_O is 0.2 eV higher than the E_O value on Pt (111) surface.[46,47] For convenience, here we shift the optimal E_O value to 0 eV and use ΔE_O to represent the difference of a given E_O value relative to this optimal reference. Thus, a catalyst with ΔE_O value closer to zero is predicted to exhibit a superior ORR activity. Since high densities of (211) and (311) surfaces were observed in STEM, we focused on these two surfaces as representatives of HIFs on the NWs. Considering that the Pt skin is formed due to near-surface compositional segregation through thermal annealing, we modeled the Pt skin with (211) and (311) facets by exchanging all Fe atoms in the top two layers with the Pt atoms in the third layer. In other words, the Pt-skin models consist of pure Pt in the top two layers, $PtFe_3$ in the third layer, and Pt_3Fe in the remaining layers. In general, both surface strain and ligand effect could influence catalytic activities. Our DFT calculations show that the lattice constant of Pt_3Fe is ≈1.5% smaller than that of Pt, thus the lattice mismatch between them could induce a compressive strain on the NW surface. To examine the strain effect

on the catalysis, we calculate ΔE_O on the surfaces under a compressive strain, ranging from 0% to 2%. To elucidate the ligand effect, we also calculated ΔE_O on the pure Pt HIFs in the absence of Fe and contrasted it to that on the Pt skin with Fe. Specifically, two typical adsorption sites on (211) and (311) surfaces were examined—the bridge site (B) at the step edge and the hollow site (H) on the facet, as shown in **Figure 4**. Previous study on a Pt nanoparticle with a diameter of 3.5 nm has found that ΔE_O values on the (111) facet and the edge of the NP are close to those on the (111) H site and the (211) B site of Pt surface, respectively.[48] Thus, we can assess the ORR activity on the NP by the corresponding activity on the Pt surface. Figure 4 summarizes all ΔE_O values discussed above. On both (211) and (311) facets of the Pt skin, ΔE_O is closer to the optimal value than that of the Pt NP, suggesting superior ORR activity on the Pt-skin z-NWs to the Pt nanoparticles, consistent with the experimental observations. The presence of HIFs enhances the ORR performance, manifested by the fact that ΔE_O on the pure Pt HIFs is closer to the optimal value than that of the Pt nanoparticle. Furthermore, the presence of Fe on the third-layers reduces the binding between the oxygen and Pt surface as indicated in Figure 4, implying that the Pt-skin NWs should also have higher ORR activities than the pure Pt NWs. Therefore, the exceptional ORR performance of the Pt-skin Pt_3Fe z-NWs stems from both the presence of the HIFs and the ligand effect. Without the protection of the Pt skin, more edge sites may be created on the surface of the pristine Pt_3Fe z-NWs due to the dissolution of Fe atoms under the electrochemical environment.[35] It is known that these edge sites have stronger Pt-O binding, which lowers the ORR activity.[49] Hence, the ORR performance on the Pt-skin z-NWs should be superior to the pristine z-NWs, consistent with the experiments.

The unique Pt-skin Pt_3Fe z-NWs/C catalyst also enables excellent catalytic activity toward the oxidation of organic molecules that are key to the liquid fuels powered fuel cell technology. Here, we used MOR and EOR as the probe reactions. **Figure 5**a shows the CVs of Pt-skin Pt_3Fe z-NWs/C, Pt_3Fe

ADVANCED
SCIENCE NEWS
www.advancedsciencenews.com

ADVANCED
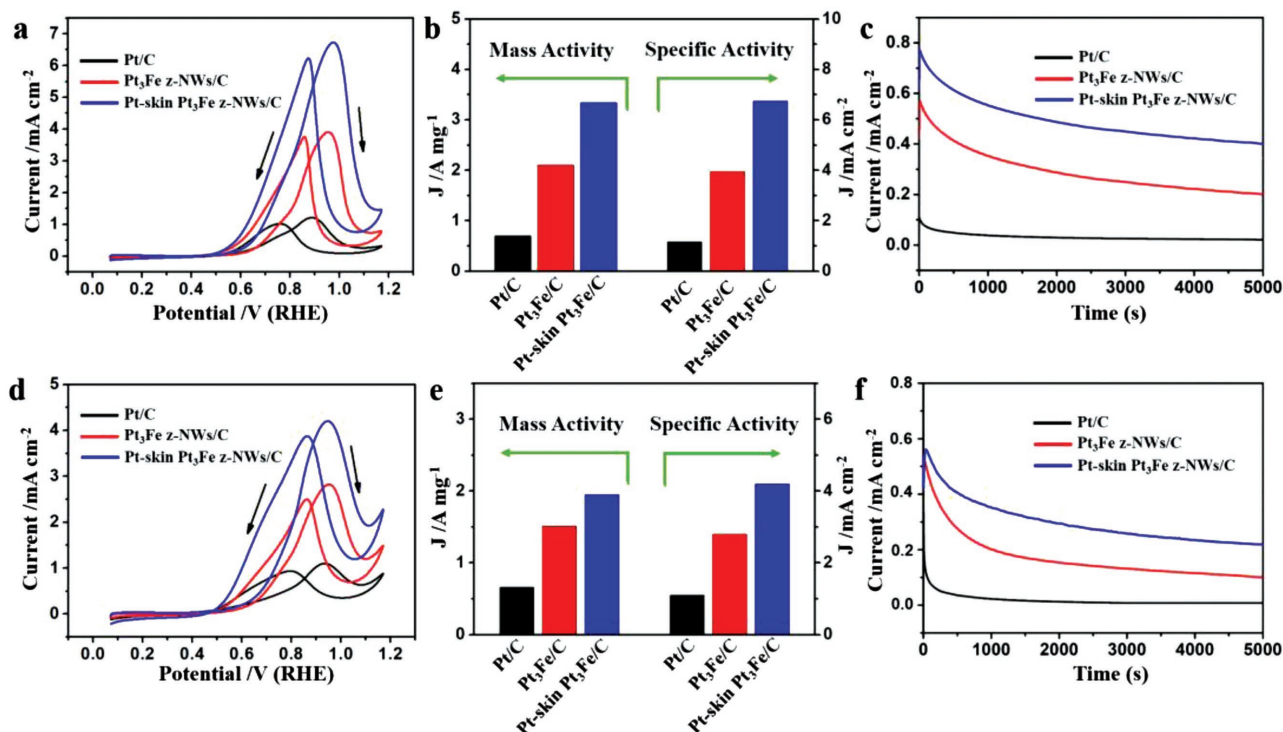MATERIALS
www.advmat.de

Figure 5. Catalytic performance for MOR and EOR. a) ECSA-normalized CVs, b) histogram of mass activity and specific activity, and c) chronoamperometric (CA) tests of various catalysts for MOR conducted in 0.1 M $HClO_4$ solution containing 0.5 M methanol. d) ECSA-normalized CVs, e) histogram of mass activity and specific activity, and f) CA tests of various catalysts for EOR in 0.1 M $HClO_4$ solution containing 0.5 M ethanol. The CA curves were recorded at a constant potential of 0.65 V versus RHE.

z-NWs/C, and Pt/C for MOR in a 0.1 M $HClO_4$ containing 0.5 M CH_3OH solution at a scan rate of 50 mV s^{-1}. We found that the anodic current for MOR of Pt-skin Pt_3Fe z-NWs/C is much higher than those of other two catalysts. Impressively, the Pt-skin Pt_3Fe z-NWs/C achieve 4.8 times higher in mass activity and 5.8 times higher in specific activity for MOR than the commercial Pt/C, respectively (Figure 5b; Table S3, Supporting Information). Chronoamperometric tests were carried out to reveal the catalytic durability. As shown in Figure 5c, after a period of 5000 s, the Pt-skin Pt_3Fe z-NWs/C enables a retention of 35.7% of the initial current density for MOR, much higher than those of the pristine Pt_3Fe z-NWs/C (21.7%) and the commercial Pt/C (9.6%), indicating excellent durability of Pt-skin structured catalyst. In terms of EOR, the Pt-skin Pt_3Fe z-NWs/C also delivers the highest catalytic activity (Figure 5d), with a mass activity of 1.95 A mg^{-1} and a specific activity of 4.3 mA cm^{-2}, respectively (Figure 5e; Table S4, Supporting Information). As displayed in Figure 5f, the Pt-skin Pt_3Fe z-NWs/C retained 27.5% of the initial current density, greater than the other two catalysts.

This work aims to create a catalytic structure that combines nanosegregated Pt-skin structure and HIFs surface for fuel cells related reactions. Although a number of studies have reported the synthesis of HIFs enclosed nanocrystals via either wet-chemical or electrochemical approach,[50–53] most of them tend to aggregate or reconstruct during the thermal treatment that is necessary to form the unique Pt-skin structure and the electrocatalytic conditions. We address this challenge by creating stable HIFs on 1D z-NWs rather than on commonly used

0D nanoparticles. First, our previous work demonstrates the excellent antiaggregation property of 1D NWs catalyst upon thermal treatment or electrochemical cycling, ascribed to their multipoint contacts with the carbon support.[34] Second, the 1D nature and large diameter of NWs can relax the high surface energy of HIFs and thus reduce the atomic mobility on the surface.[41] Indeed, we do not observe any changes in the morphology of Pt_3Fe z-NWs before and after thermal treatment (Figure 2a). Spherical aberration STEM (Figure 2b,d), combined with high-resolution EDS elemental mapping and line scan (Figure 2e) and the distinct ratio between ECSA$_{CO}$ and ECSA$_{Hupd}$ (Table S1, Supporting Information) of Pt-skin Pt_3Fe z-NWs/C confirms the existence of desired HIF Pt-skin structure.[23] The ORR activity of Pt-skin Pt_3Fe z-NWs/C nearly doubles that of pristine Pt_3Fe z-NWs/C, undoubtedly confirming the essential role of Pt-skin structure in promoting ORR electrocatalysis in HIFs catalytic system (Table S5, Supporting Information). As suggested by Stamenkovic et al., the formation of Pt-skin structure can lower the surface coverage of spectator oxygenated species (such as OH_{ad}) on catalysts and thus increase the number of active sites for O_2 adsorption and subsequently reduction.[16] In addition, owing to the presence of Pt-skin and 1D structure, the Pt-skin Pt_3Fe z-NWs not only show high resistance to morphology transformation, but also protect the beneficial Fe atoms from dissolution, thus largely maintain the active sites during operating condition.

In summary, we present a proof-of-concept study on promoting fuel cells related electrocatalysis by creating extremely stable HIF Pt skin on 1D Pt_3Fe z-NWs. These key structural

features have been verified by aberration corrected STEM, elemental mapping, line scan, and the ratio of $ECSA_{CO}/ECSA_{Hupd}$. The unique 1D nanostructure enables an unprecedented activity toward the electroreduction of oxygen in all reported PtFe-based ORR catalysts, along with much enhanced MOR and EOR activities over the benchmark Pt/C catalyst. DFT calculations reveal that the activity enhancement of the Pt-skin Pt_3Fe z-NWs/C derives from a combination of exposed HIFs and the formation of Pt-skin structure, leading to the optimal oxygen adsorption energy. Impressively, little activity decay and negligible morphology transformation of Pt-skin Pt_3Fe z-NWs catalyst are observed after 50 000 potential cycles. In addition, the Pt-skin Pt_3Fe z-NWs/C also showed impressively electroanalysis performance toward the detection of H_2O_2 (Figure S21, Supporting Information). Our findings can be also extended to other PtM catalytic systems, and inspire future efforts to advancing Pt-based nanocatalysts by going from low index facets to HIFs.

Supporting Information

Supporting Information is available from the Wiley Online Library or from the author.

Conflict of Interest

The authors declare no conflict of interest.

[1] M. K. Debe, *Nature* **2012**, *486*, 43.
[2] O. Gröger, H. A. Gasteiger, J.-P. Suchsland, *J. Electrochem. Soc.* **2015**, *162*, A2605.
[3] I. E. Stephens, J. Rossmeisl, I. Chorkendorff, *Science* **2016**, *354*, 1378.
[4] Y. J. Wang, N. Zhao, B. Fang, H. Li, X. T. Bi, H. Wang, *Chem. Rev.* **2015**, *115*, 3433.
[5] H. A. Gasteiger, S. S. Kocha, B. Sompalli, F. T. Wagner, *Appl. Catal., B* **2005**, *56*, 9.
[6] M. Shao, Q. Chang, J. P. Dodelet, R. Chenitz, *Chem. Rev.* **2016**, *116*, 3594.
[7] J. Wu, H. Yang, *Acc. Chem. Res.* **2013**, *46*, 1848.
[8] M. Oezaslan, F. Hasché, P. Strasser, *J. Phys. Chem. Lett.* **2013**, *4*, 3273.
[9] I. Stephens, A. S. Bondarenko, U. Grønbjerg, J. Rossmeisl, I. Chorkendorff, *Energy Environ. Sci.* **2012**, *5*, 6744.
[10] Z. W. Seh, J. Kibsgaard, C. F. Dickens, I. Chorkendorff, J. K. Norskov, T. F. Jaramillo, *Science* **2017**, *355*, eaad4998.
[11] Y. Xia, X. Yang, *Acc. Chem. Res.* **2017**, *50*, 450.
[12] W. Yu, M. D. Porosoff, J. G. Chen, *Chem. Rev.* **2012**, *112*, 5780.
[13] I. E. Stephens, A. S. Bondarenko, F. J. Perez-Alonso, F. Calle-Vallejo, L. Bech, T. P. Johansson, A. K. Jepsen, R. Frydendal, B. P. Knudsen, J. Rossmeisl, I. Chorkendorff, *J. Am. Chem. Soc.* **2011**, *133*, 5485.
[14] V. Stamenkovic, B. S. Mun, K. J. Mayrhofer, P. N. Ross, N. M. Markovic, J. Rossmeisl, J. Greeley, J. K. Norskov, *Angew. Chem., Int. Ed. Engl.* **2006**, *45*, 2897.
[15] H. Yang, *Angew. Chem., Int. Ed. Engl.* **2011**, *50*, 2674.
[16] V. R. Stamenkovic, B. Fowler, B. S. Mun, G. Wang, P. N. Ross, C. A. Lucas, N. M. Markovic, *Science* **2007**, *315*, 493.
[17] X. Q. Huang, Z. P. Zhao, L. Cao, Y. Chen, E. B. Zhu, Z. Y. Lin, M. F. Li, A. M. Yan, A. Zettl, Y. M. Wang, X. F. Duan, T. Mueller, Y. Huang, *Science* **2015**, *348*, 1230.
[18] X. Huang, Z. Zhao, Y. Chen, E. Zhu, M. Li, X. Duan, Y. Huang, *Energy Environ. Sci.* **2014**, *7*, 2957.
[19] S.-I. Choi, S. Xie, M. Shao, J. H. Odell, N. Lu, H.-C. Peng, L. Protsailo, S. Guerrero, J. Park, X. Xia, J. Wang, M. J. Kim, Y. Xia, *Nano Lett.* **2013**, *13*, 3420.
[20] C. Cui, L. Gan, H. H. Li, S. H. Yu, M. Heggen, P. Strasser, *Nano Lett.* **2012**, *12*, 5885.
[21] J. Zhang, H. Yang, J. Fang, S. Zou, *Nano Lett.* **2010**, *10*, 638.
[22] J. Wu, L. Qi, H. You, A. Gross, J. Li, H. Yang, *J. Am. Chem. Soc.* **2012**, *134*, 11880.
[23] C. Chen, Y. Kang, Z. Huo, Z. Zhu, W. Huang, H. L. Xin, J. D. Snyder, D. Li, J. A. Herron, M. Mavrikakis, M. Chi, K. L. More, Y. Li, N. M. Markovic, G. A. Somorjai, P. Yang, V. R. Stamenkovic, *Science* **2014**, *343*, 1339.
[24] P. Strasser, *Science* **2015**, *349*, 379.
[25] N. Becknell, Y. Son, D. Kim, D. Li, Y. Yu, Z. Niu, T. Lei, B. T. Sneed, K. L. More, N. M. Markovic, V. R. Stamenkovic, P. Yang, *J. Am. Chem. Soc.* **2017**, *139*, 11678.
[26] S. Kobayashi, M. Wakisaka, D. A. Tryk, A. Iiyama, H. Uchida, *J. Phys. Chem. C* **2017**, *121*, 11234.
[27] N. Hoshi, M. Nakamura, A. Hitotsuyanagi, *Electrochim. Acta* **2013**, *112*, 899.
[28] A. Kuzume, E. Herrero, J. M. Feliu, *J. Electroanal. Chem.* **2007**, *599*, 333.
[29] V. R. Stamenkovic, B. S. Mun, K. J. Mayrhofer, P. N. Ross, N. M. Markovic, *J. Am. Chem. Soc.* **2006**, *128*, 8813.
[30] Y. Xia, Y. Xiong, B. Lim, S. E. Skrabalak, *Angew. Chem., Int. Ed.* **2009**, *48*, 60.
[31] L. Bu, J. Ding, S. Guo, X. Zhang, D. Su, X. Zhu, J. Yao, J. Guo, G. Lu, X. Huang, *Adv. Mater.* **2015**, *27*, 7204.
[32] S. Sun, C. B. Murray, D. Weller, L. Folks, A. Moser, *Science* **2000**, *287*, 1989.
[33] B. Lim, M. Jiang, P. H. Camargo, E. C. Cho, J. Tao, X. Lu, Y. Zhu, Y. Xia, *Science* **2009**, *324*, 1302.
[34] L. Bu, S. Guo, X. Zhang, X. Shen, D. Su, G. Lu, X. Zhu, J. Yao, J. Guo, X. Huang, *Nat. Commun.* **2016**, *7*, 11850.
[35] V. R. Stamenkovic, B. S. Mun, M. Arenz, K. J. Mayrhofer, C. A. Lucas, G. Wang, P. N. Ross, N. M. Markovic, *Nat. Mater.* **2007**, *6*, 241.
[36] S. Chen, P. J. Ferreira, W. Sheng, N. Yabuuchi, L. F. Allard, Y. Shao-Horn, *J. Am. Chem. Soc.* **2008**, *130*, 13818.
[37] S. Guo, D. Li, H. Zhu, S. Zhang, N. M. Markovic, V. R. Stamenkovic, S. Sun, *Angew. Chem., Int. Ed. Engl.* **2013**, *52*, 3465.

[38] D. Li, C. Wang, D. Tripkovic, S. Sun, N. M. Markovic, V. R. Stamenkovic, *ACS Catal.* **2012**, *2*, 1358.

[39] D. F. Van der Vliet, C. Wang, D. Li, A. P. Paulikas, J. Greeley, R. B. Rankin, D. Strmcnik, D. Tripkovic, N. M. Markovic, V. R. Stamenkovic, *Angew. Chem., Int. Ed.* **2012**, *51*, 3139.

[40] M. Shao, J. H. Odell, S.-I. Choi, Y. Xia, *Electrochem. Commun.* **2013**, *31*, 46.

[41] K. D. Gilroy, A. Ruditskiy, H. C. Peng, D. Qin, Y. Xia, *Chem. Rev.* **2016**, *116*, 10414.

[42] M. Li, Z. Zhao, T. Cheng, A. Fortunelli, C. Y. Chen, R. Yu, Q. Zhang, L. Gu, B. V. Merinov, Z. Lin, E. Zhu, T. Yu, Q. Jia, J. Guo, L. Zhang, W. A. Goddard, Y. Huang, X. Duan, *Science* **2016**, *354*, 1414.

[43] K. Jiang, D. Zhao, S. Guo, X. Zhang, X. Zhu, J. Guo, G. Lu, X. Huang, *Sci. Adv.* **2017**, *3*, e1601705.

[44] S. Zhang, X. Zhang, G. Jiang, H. Zhu, S. Guo, D. Su, G. Lu, S. Sun, *J. Am. Chem. Soc.* **2014**, *136*, 7734.

[45] D. Wang, H. L. Xin, R. Hovden, H. Wang, Y. Yu, D. A. Muller, F. J. DiSalvo, H. D. Abruna, *Nat. Mater.* **2013**, *12*, 81.

[46] X. Huang, S. Tang, X. Mu, Y. Dai, G. Chen, Z. Zhou, F. Ruan, Z. Yang, N. Zheng, *Nat. Nanotechnol.* **2011**, *6*, 28.

[47] R. L. Penn, J. F. Banfield, *Science* **1998**, *281*, 969.

[48] S. Kuhl, H. Heyen, P. Strasser, *ECS Trans.* **2016**, *75*, 723.

[49] E. Gonzalez, J. Arbiol, V. F. Puntes, *Science* **2011**, *334*, 1377.

[50] L. Zhang, D. Chen, Z. Jiang, J. Zhang, S. Xie, Q. Kuang, Z. Xie, L. Zheng, *Nano Res.* **2012**, *5*, 181.

[51] N. Tian, Z. Y. Zhou, S. G. Sun, Y. Ding, Z. L. Wang, *Science* **2007**, *316*, 732.

[52] T. Sheng, N. Tian, Z.-Y. Zhou, W.-F. Lin, S.-G. Sun, *ACS Energy Lett.* **2017**, *2*, 1892.

[53] L. Huang, X. Zhang, Y. Han, Q. Wang, Y. Fang, S. Dong, *Chem. Mater.* **2017**, *29*, 4557.